PHYSICAL REVIEW E **70**, 066139 (2004)

Microscopic structure, dynamics, and wear at metal-metal interfaces in sliding contact

Igor Stankovic* and Siegfried Hess
Institut für Theoretische Physik, PN 7-1, Fakultät II, Technische Universität Berlin, D-10623 Berlin, Germany

Martin Kröger
Polymer Physics, ETH Zürich, Wolfgang-Pauli-Str. 10, CH-8093 Zürich, Switzerland

(Received 25 March 2004; revised manuscript received 14 September 2004; published 27 December 2004)

The "generic embedded atom model" (GEAM) has been investigated recently [Phys. Rev. E **69**, 021509 (2004)] to analyze the qualitative equilibrium and nonequilibrium properties of bulk metals in both undeformed and shear deformed states. In the present work, a natural extension of the GEAM is proposed and applied to characterize the microscopic structure, dynamics, and wear at clean commensurate metal$_A$-metal$_A$ and metal$_A$-metal$_B$ sliding interfaces. Nonequilibrium molecular dynamics simulation, used as a GEAM solver, reveals that the dynamics of dislocations, crystalline domains, and related flow behaviors (stress tensor, shear moduli) are coupled. The rotation of crystal domains is detected to trigger material mixing at the interface in early stages of sliding. Further, we study the dependence of structural changes in inhomogeneous metal interfaces on the relevant model parameters. A relation is established between shear moduli, effective shear rate, and shear stress across the interface.

DOI: 10.1103/PhysRevE.70.066139 PACS number(s): 81.40.Pq, 62.20.Fe, 68.35.Af, 07.05.Tp

I. INTRODUCTION

The dry sliding friction between atomically flat commensurate and incommensurate surfaces are fundamental types of friction in the tribological sciences. When two unpolished solid surfaces get in contact, either by touching, or by applying a moderate load, they actually interact only over a small fraction of their total macroscopic area of contact. This load-bearing area consists of a number of asperities since microscopic roughness is strictly unavoidable. Asperities are the spots of exclusive relevance for the understanding of the submacroscopic mechanisms in dry solid friction and adhesive wear. The variety of processes taking place at friction surfaces (such as inhomogeneous plastic deformation of a subsurface layer, phase transformations, material transfer, mechanical alloying) render it difficult to develop a general approach for describing the microscopic structure, dynamics, and wear in the course of rubbing [1–4]. With the development of atomic force microscopy, tribology has reached the nanoscale [5,6]. But the atomic friction microscope has its own limits, in particular for "high speed" friction, and it is restricted to extremely sharp tips. This explains the interest for numerical simulations of friction. Recent theoretical studies using atomistic models and molecular dynamics simulations have provided a better insight into friction on the nanoscale. Such studies offer detailed information about the influence of solid and fluid thin films on static friction, phonon dynamics, and the transition from stick slip to smooth sliding [7–10]. A rather complete picture about dynamical dissipation during slip-stick motion and the solid sliding regime emerged [10–12]. On the other hand, the relationship between material properties, long range elastic deformations, intermediate structure, and material transfer at the interface between identical and different metals is less well understood [13,14].

The present study focuses on the effect of the choice of interfacial parameters on the microscopic dynamics and structure in order to characterize a simple embedded atoms model for metals, and to explore its range of applicability. To this end we consider a stationary shear deformation between metals sliding past each other with large relative speeds. We restrict ourself to the study of metal-metal contacts, where the effect of the interfacial parameter is most transparent although the choice of parameters does not reflect any particular chosen "real" situation (we will come back to this point in Sec. II E). The results help to predict the microscopic behaviors when two blocks of metal with similar lattice constants but different structural and mechanical properties come in direct solid contact. The present study focuses on the role of dislocations, created under steady shear deformation, for the flow profile, local structure, and pressure tensor. It is thus complementary to recent large-scale simulations of nanocrystalline metals where for small strains (small time windows) the generation and dynamics of dislocations had been studied in detail; see Refs. [15–18].

For the interactions between metal atoms we adopt an extension of potentials used in Refs. [14,19]. For this model, the total electron density is approximated by a linear superposition of contributions from individual atoms. The electron (or embedding) density at the center of mass of any atom is expressed as a sum over densities from neighboring sites. In addition, there is an energy contribution due to the ion-ion interactions. Accordingly, the embedded atoms energy is expressed as

$$E = \sum_{i=1}^{N} \left(\mathcal{F}(\rho_i) + \sum_{j>i}^{N} e_{ij} \mathcal{U}(r^{ij}) \right), \tag{1}$$

---

*Corresponding author.
Electronic address: stankovic@itp.physik.tu-berlin.de

TABLE I. Experimental values [29–33] for Cu, Ni, Ag, Au, Pd, and Pt: lattice constant a_0, particle number density n, energy per particle (cohesive energy) E_{coh}, bulk B, and shear G moduli, along with heats of solution ΔE for given host-impurity pairs. The stacking fault energy γ_{sf} and unstable stacking fault energy γ_{sf} are obtained with tight-binding and first-principles calculations in Refs. [34,35]. For GEAM metal constitutive properties are given in both in "real" (dimensional), and reduced (adimensional) units (bottom row).

Metal	a_0 (nm)	n (nm^{-3})	E_{coh} (eV)	B (GPa)	G (GPa)	γ_{sf} (eV/nm^2)	γ_{usf} (eV/nm^2)	$\lvert\gamma_{\text{usf}}-\gamma_{\text{sf}}\rvert$ (eV/nm^2)	ΔE (host impurity) (eV)
Cu	0.362	85.9	3.50	142	59.3	0.4	1.25	0.85	0.03 (Cu—Ni)
Ni	0.352	84.6	4.45	183	94.3	1.14	1.48	0.34	0.11 (Ni—Cu)
Ag	0.409	58.0	2.95	101	33.5	0.11	0.58	0.47	−0.19 (Ag—Au)
Au	0.408	58.5	3.81	174	30.7	0.23	0.69	0.46	−0.16 (Au—Ag)
Pd	0.389	68.0	3.91	195	54.3	1.06	1.95	0.89	−0.04 (Pd—Pt)
Pt	0.392	66.4	5.77	283	65.1	1.68	2.45	0.77	−0.21 (Pt—Pd)
GEAM	0.271	72.5	1.91	179	52.7	0	1.00	1.00	(dimensional)
	1.12	0.993	0.552	4.442	1.309	0	0.021	0.021	(adimensional)

$$\rho_i = \sum_{j\neq i}^{N} w_{ij} w(r^{ij}) + w(0), \tag{2}$$

where E is the total potential energy of the system made up of N atoms, and ρ_i is local embedding density constructed from the radial distances $r^{ij}=|\boldsymbol{r}_i-\boldsymbol{r}_j|$ of atoms $\{j\}$ "surrounding" atom i located at position $\boldsymbol{r}_i$. The model requires the choice of a radially symmetric weighting function $w(r)$, and $w(0)$ is the local embedding density of a solitary atom. The embedding functional $\mathcal{F}(\rho_i)$ constitutes the energy of a particle represented by the embedding density ρ_i, and the radially symmetric two-body interaction is modelled through the potential $\mathcal{U}$. The (effectively many-body) model potential in Eq. (1) serves to model a variety of metal properties. Compared with the model described in Ref. [14], the coefficients e_{ij} and w_{ij} are newly introduced to model the properties at the interface between two (or more) metal species in contact. They allow us to specify the strength of interaction between atoms belonging to the same and to different materials. Since we are going to deal with two metals (type A and B) in contact throughout the manuscript, the coefficients e_{ij} can take one of the three values e_{AA}, e_{BB}, or $e_{\text{AB}}=e_{\text{BA}}$, depending on the species to which atoms i and j belong (either A or B). The same applies to the w_{ij} interaction strengths. As will be shown in Sec. II D, these coefficients affect the heat of solution and hardness of the material's interface. By default, and if not otherwise mentioned, all interaction strength parameters are set to unity. Thus the default is a (bulk) system without marked interface.

II. GENERIC EMBEDDED ATOMS (GEAM) MODEL

A. Definition

A particular choice for the model function(al)s $\mathcal{U}$, w, and $\mathcal{F}$ has been motivated in Ref. [19], and leads to the generic embedded atom model (GEAM) metal. For this model, both the binary interaction potential and weight function are polynomials in the interparticle distance r:

$$\mathcal{U}(r) = \frac{\phi_0}{r_0^4}[3(r_{\text{cut}}-r)^4 - 4(r_{\text{cut}}-r_{\text{min}})(r_{\text{cut}}-r)^3], \tag{3}$$

$$w(r) = w_0\left(1+3\frac{r}{r_{\text{cut}}}\right)\left(1-\frac{r}{r_{\text{cut}}}\right)^3, \tag{4}$$

for $r \leqslant r_{\text{cut}}$, and $\mathcal{U}(r)=0$, $w(r)=0$ otherwise, with an energy scale ϕ_0, a length scale r_0, an interaction range r_{min}, a cutoff radius r_{cut}, and a pre-factor obtained by normalizing the weight function, $w_0=w(0)=105/(16\pi r_{\text{cut}}^3)$. The parabolic GEAM embedding functional reads

$$\mathcal{F}(\rho) = F_2\phi_0 r_0^6[(\rho-\rho_{\text{des}})^2 - (w_0-\rho_{\text{des}})^2] + \cdots, \tag{5}$$

where ρ_{des} is the desired embedding density, and $F_2=1$ is the embedding strength of GEAM. Odd terms in embedding density do not occur in this "expansion" because they create aphysical, destabilizing forces. A linear term $\Delta\rho=(\rho-\rho_{\text{des}})$ is not present because it could be adsorbed by a modified pair potential $\mathcal{U}$. The dots in Eq. (5) represent higher-order terms in $\Delta\rho$ which may be considered in order to obtain more than a qualitative agreement between theoretical and experimental values for cohesive energy with respect to the quantities listed in Table I. The desired GEAM embedding density is set to $\rho_{\text{des}}=r_0^{-3}$. The particle number density is denoted as $n\equiv N/V$. The minimum of the binary potential is located at the distance $r=r_{\text{min}}=2^{1/6}r_0\approx 1.12r_0$ (as for a Lennard-Jones potential), the cutoff distance is set to $r_{\text{cut}}=1.6r_0$.

B. Crystal structure

For a system made of particles occupying ideal lattice sites (or any other configuration) the cohesive energy, or energy per particle, $E_{\text{c}}=E/N$ is calculated from Eq. (1). The variation of this energy subject to a uniaxial volume conserving deformation referred to as Bain deformation [20,21], parametrized by the ratio $a_{[100]}/a_{[010]}$ between sides of a conventional bcc cubic cell [22], is presented in Fig. 1. Under Bain transformation the system transforms from a bcc structure $a_{[100]}/a_{[010]}=1$ into an fcc structure at $a_{[100]}/a_{[010]}\approx 1.414$. Both fcc and bcc structures correspond to local

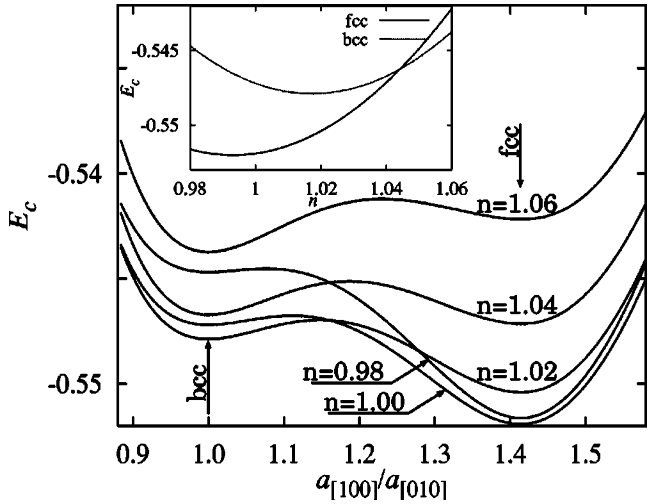

FIG. 1. Cohesive energy vs ratio $a_{[100]}/a_{[010]}$ during volume conserving tetragonal Bain transformation, described in Sec. II B. The transformation of the ideal GEAM metal lattice is presented for global number densities $n=0.98,\ldots,1.06$. The bcc structure occurs at $a_{[100]}/a_{[010]}\approx 1$ and the fcc at $a_{[100]}/a_{[010]}=1.414$. The inset shows the effect of density n on the cohesive energy for ideal fcc and bcc structures. All quantities are given in dimensionless reduced units; cf. Sec. II E and Table I.

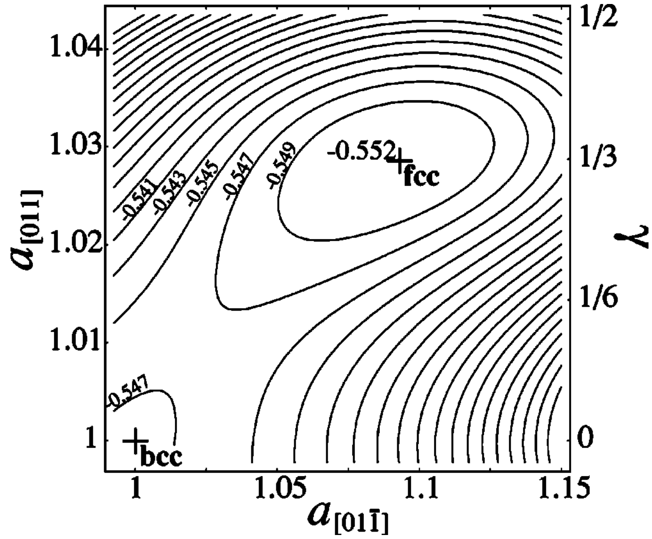

FIG. 2. Cohesive energy contours in the vicinity of the Burgers transformation path; cf. Sec. II B. The system is simultaneously deformed ($a_{[01\bar{1}]}$) in [011] direction and sheared by an amount γ along the $[01\bar{1}]$ direction/gradient direction [011]. For a Burgers transformation [23] the original bcc structure is transformed into the fcc structure after being deformed by $\approx$9, 3, and -11 % along the $[01\bar{1}]$, [011], and [100] directions, respectively, and subsequently sheared with $\gamma=1/3$.

minima of the cohesive energy with respect to this ratio. During Bain transformation the bcc structure contracts along [010] and [001] directions by $\approx -11\%$ and expands along the [100] direction by about 21%, so that these axes transform to $[01\bar{1}]$, [011], and [100] axes of the fcc structure. Burgers [23] suggested a mechanism for the bcc to hcp transformation that can be also applied to the transformation of bcc into fcc structure. For this transformation mechanism the original bcc structure is deformed along the $[01\bar{1}]$, [011], and [100] directions for $\approx$9, 3, and -11 %, respectively, and subsequently sheared (with $\gamma=1/3$) in shear direction $[01\bar{1}]$/gradient direction [011]; see Fig. 2. Unexpected at first glance, the energy barrier between fcc and bcc structures is similar for both structure transformation mechanisms, cf. Figs. 1 and 2. Yet the Bain deformation induces a relative shift of layers of atoms in the crystal, similar to the shear in the Burgers mechanism and therefore the degrees involved in transformation of structure are very similar for these two mechanisms, as further discussed in Ref. [24].

For GEAM, both fcc and hcp structures are ground state structures, i.e., structures with minimum energy per particle. This results in a zero stacking fault energy γ_{sf} and energy difference between fcc and hcp structure. For this reason, one might expect pronounced defects—stacking faults and twins—in a GEAM metal under shear "flow," i.e., shear deformation at constant deformation rate. This need not to be the case in the strong flow regime: (i) Stacking fault is created when two semi-infinite blocks of fcc crystal are sheared on the (111) plane along a $[1\bar{1}0]$ direction. Along this path, the system has to first pass through an energy barrier referred here as the unstable stacking fault energy γ_{usf}. The stacking fault results in the formation of a hcp plane inside the fcc structure. Recent studies suggest that the dislocation activity is not determined by the value of the stacking fault energy alone. The difference between stacking fault energy and unstable stacking fault energy $|\gamma_{\mathrm{usf}}-\gamma_{\mathrm{sf}}|$ has been included into the description [15–17,35] For the case of GEAM, the difference $|\gamma_{\mathrm{usf}}-\gamma_{\mathrm{sf}}|$ is comparable in magnitude with the value observed in metals with low γ_{sf} values; see Table I. (ii) In the strong shear flow regime the thermal energy of the particles is comparable, but smaller than the magnitude of the potential barrier γ_{usf}. Therefore atoms in fcc single crystals subjected to strong shear deformation easily slide into their nearest potential minima, creating stacking faults.

In order to estimate the effect of the given structure (fcc, bcc) on the stability of systems for which the temperature and the volume are fixed at prescribed values, one has to consider the Helmholtz free energy $F(T,V)=U-TS$ [25]. The internal energy U of the system is defined as a sum of potential and kinetic energies, cf. Sec. III, and thus directly available from our molecular dynamics (MD) simulations. Concerning the absolute entropy S, however, there is no such basic recipe. The "thermodynamic integration" technique provides a workaround and estimates the difference between free energies of two phases. The Gibbs relation

$$dF = -PdV - SdT \tag{6}$$

quantifies how changes in volume and temperature affect the Helmholtz free energy. The basic idea is to transform, via MD, the fcc solid into a bcc solid along the Bain transformation path at constant temperature [26,27]. Then, the change of the free energy dF is

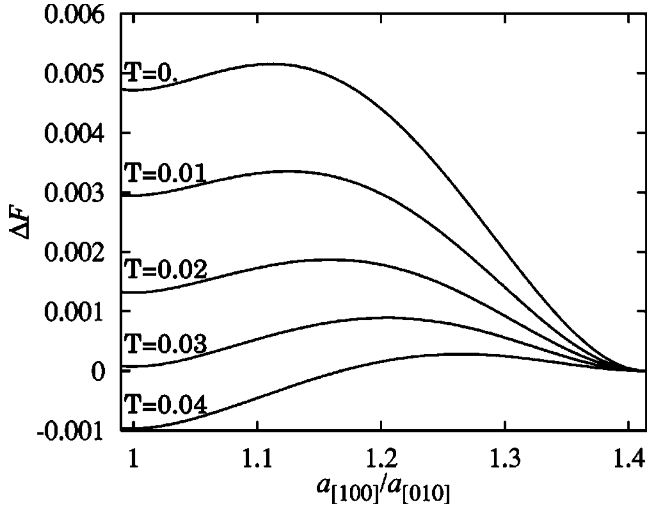

FIG. 3. Change of the free energy vs ratio $a_{[100]}/a_{[010]}$ during uniaxial volume conserving Bain transformation. The transformation of the ideal GEAM metal lattice is presented for temperatures $T=0.01,\ldots,0.04$. Both fcc and bcc structures correspond to local minima of the cohesive energy with respect to the ratio $a_{[100]}/a_{[010]}$.

$$dF = -P_{xx}A_x dx - P_{yy}A_y dy - P_{zz}A_z dz, \qquad (7)$$

where P_i are diagonal, Cartesian components of the pressure tensor $(i=xx,yy,zz)$ and A_λ denote surface areas orthogonal to these directions. Figure 3 shows the change of the specific free energy $\Delta F/N$ along the Bain transformation path at number density $n=1$ and temperatures $T=0,\ldots,0.04$, calculated via MD.

In the limit of low temperatures, the structure with the larger internal energy is the thermodynamically stable one. Here the bcc structure $(a_{[100]}/a_{[010]}=1)$ corresponds to a local, the fcc structure to global minimum. A larger entropy for the bcc structure compared to the fcc structure is expected, since bcc is less densely packed. Accordingly, the free energy of a bcc structure should decrease faster with increasing temperature. At sufficiently high temperature the local minimum at $a_{[100]}/a_{[010]}=1$ can evolve into a global one. This is what we indeed observe for the GEAM metal, cf. Fig. 3, for temperatures $T>0.03$. In Fig. 4, thermodynamical integration is applied to calculate the structural phase diagram for GEAM in the temperature-density plane. The diagram shows regions where bcc and fcc structures are energetically favored, and data for two values of the two body interaction parameter $e_{\mathrm{AA}}=0.5,1.0$. The thermodynamical integration also provides the size of the potential barrier between two structures along the transformation path. This barrier is small in magnitude $(\Delta \approx 4\times 10^{-4})$ compared with thermal fluctuations at room temperature. Nevertheless, the bulk material stays in the bcc structure after rapid cooling since the structural transformation away from this state would involve collective motions of atoms. The bulk material, free of defects, cannot cross this barrier due to the thermal fluctuations even at high temperatures. Under shear flow, however, the material can sufficiently accumulate strain energy and cross this barrier, while relaxing to an energetically more preferred state as soon as the external field is released.

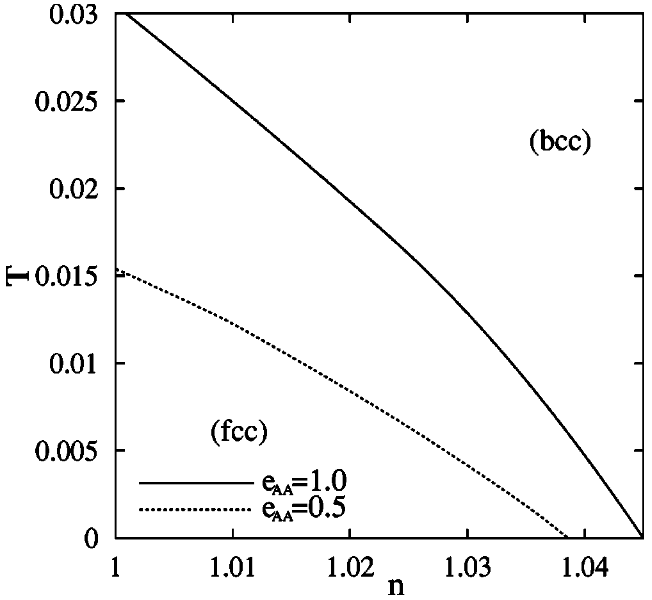

FIG. 4. Structural phase diagram of GEAM in the temperature-density plane calculated via thermodynamical integration from NEMD simulation data. The curves separate densities and temperatures where bcc and fcc structures are energetically favored for two values of the two body interaction parameter $e_{\mathrm{AA}}=0.5$ (dashed line) and 1.0 (bold). All quantities are given in dimensionless reduced units.

C. Bulk characteristics

The pressure and the elastic modulus tensor is to be obtained using the virial expressions [14,28] from analytical calculations and also from nonequilibrium molecular dynamics (NEMD), by which the GEAM model is solved numerically (cf. Sec. III). The symmetric traceless (anisotropic) pressure tensor has five independent components. In the special case of simple shear flow with velocity in the x direction and velocity gradient in the y direction only three independent components have to be considered (as long as symmetry is not broken in an average sense). Let us denote them conveniently as $p_{+,-,0}$, where $p_+ \equiv (P_{yx}+P_{xy})/2$ corresponds to a shear pressure, two normal pressure differences are $p_- \equiv (P_{xx}-P_{yy})/2$, and $p_0 \equiv [2P_{zz}-(P_{xx}+P_{yy})]/4$, respectively. The scalar (isotropic) pressure p^{iso} is the trace of the total pressure tensor divided by the spatial dimension, $p^{\mathrm{iso}} = P_{\mu\mu}/3$. Note that the "stress tensor" is identical with the pressure tensor except for its sign, i.e., $-p_+$ is the shear stress.

First, we extract these pressure tensor components and the cohesive energy in the limit of low temperatures in two cases: (i) shear direction [100]/gradient direction [010], and (ii) shear direction $[\bar{1}10]$/gradient direction [111]. In the former case the distance between the two minima corresponds to a shear deformation $\gamma=2$, in the latter case the same distance corresponds to $\gamma=\sqrt{3/2}$. In the undeformed state $(\gamma=0)$ particles occupy ideal lattice sites, i.e., are located in a position of minimum potential energy. The cohe-

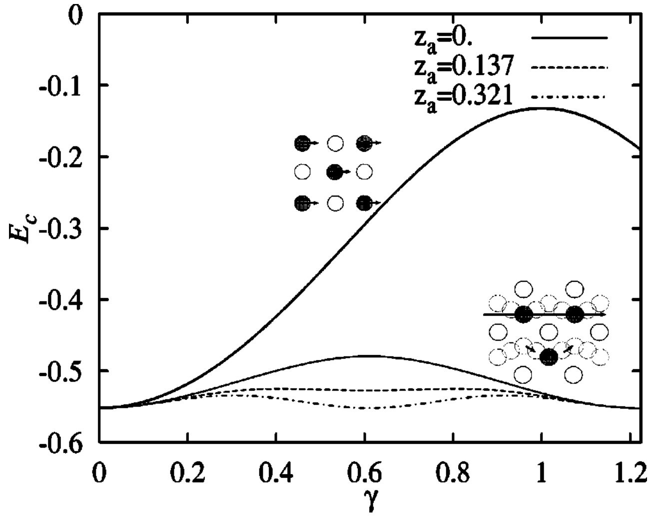

FIG. 5. Shearing of the ideal fcc crystal in the limit of low temperatures. The change of the cohesive energy (E_{coh}) with the increasing shear deformation (γ) is presented for shear direction [100]/gradient direction [010] (thick curves, upper inset) and shear direction $[1\bar{1}0]$/gradient direction [111] (thin curves, lower inset). In the latter case, sinusoidal trajectories with amplitude $z_a=0$, 0.137, and 0.321 in vorticity direction $[22\bar{1}]$ and possessing a wave length equivalent with the distance between two successive potential minima are assumed.

sive energy E_c increases with shear deformation until an unstable equilibrium is reached, cf. Fig. 5. The corresponding shear stresses are given in Fig. 6. A system with bcc or fcc structure produces maximum shear stress and maximum resistance to shear in shear direction [100]/gradient direction [010], where particles have to cross the highest potential barrier. The fcc system, when sheared along the $[1\bar{1}0]$ direction/gradient direction [111] of the crystal, has minimal resistance. Particles are then stacked within densely packed hexagonal layers corresponding to the (111) plane of the fcc crystal structure. The shear stress and the height of the potential barrier are further reduced through collective zig-zag movements of hexagonal layers within the plane; see Fig. 6.

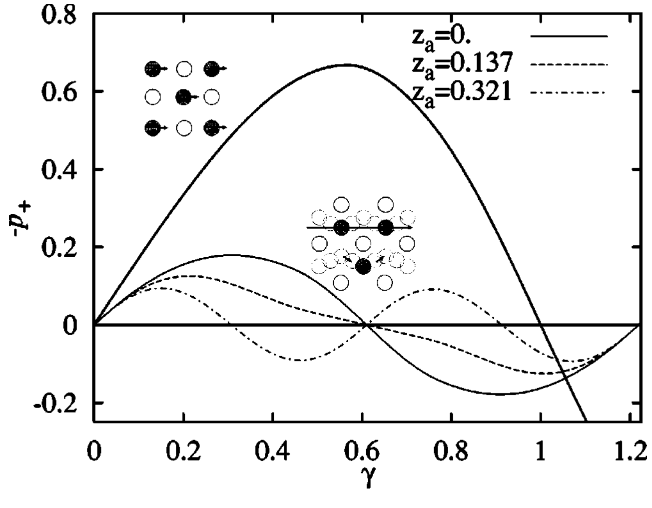

FIG. 6. Shear stress ($-p_+$) vs shear deformation (γ) for shear direction [100]/gradient direction [010] (ticker curve, upper inset) and shear direction $[1\bar{1}0]$/gradient direction [111] (thinner curves, lower inset). In the latter case, particles follow sinusoidal trajectories with amplitude z_a in vorticity direction $[22\bar{1}]$ and a wave length equivalent to the distance between two potential minima. At $\gamma=0$ particles occupy ideal fcc lattice sites.

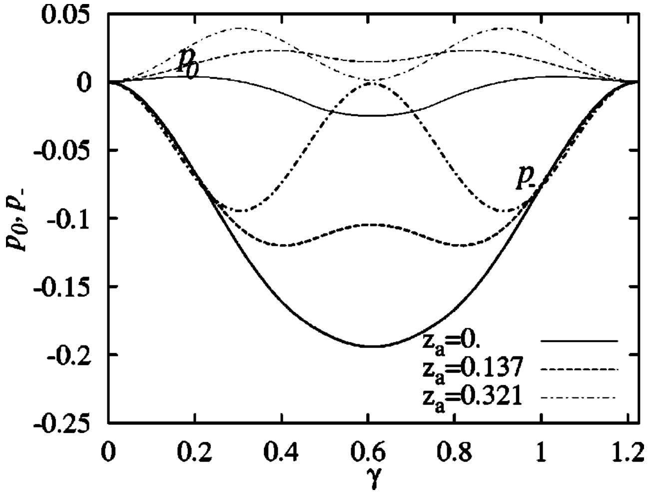

FIG. 7. Normal pressure differences p_- (ticker curves) and p_0 (thinner curves) vs shear deformation (γ) for shear direction $[1\bar{1}0]$/gradient direction [111] in the low-temperature limit; cf. Sec. IV A. Particles follow sinusoidal trajectories with amplitudes z_a $=0$, 0.137, and 0.321 in vorticity direction $[22\bar{1}]$ and a wavelength equivalent to the distance between two potential minima. Prior to the onset of shear particles occupy ideal fcc lattice sites.

Next, we assume sinusoidal trajectories between two potential energy minima with amplitude z_a in the vorticity direction $[22\bar{1}]$ in order to rigorously study the influence of zigzag motion. For $z_a=0.321$, the trajectory goes through side minimum. In this case, the height of potential barrier and the shear stress are reduced to a quarter of their values for the straight trajectory ($z_a=0$). The normal pressure differences p_0 and p_- change their signs upon increasing the amplitude z_a, as demonstrated in Fig. 7.

In the limit of low temperatures the simple GEAM yields expressions for several constitutive properties without approximations with computational effort of order N; cf. Ref. [14]. The elastic coefficients—bulk modulus B, average shear moduli G, C_{44} and $\widetilde{C}_{44}=(C_{11}-C_{12})/2$—depend on the second derivative of the free energy for a nearest neighbor model [14]. The second order term in the embedding functional, Eq. (5) without dots, mostly determines the values of the elasticity coefficients including B, C_{11}, and C_{12} characterizing the response of GEAM on volume changes, since the embedding density is usually very close to the desired embedding density. The orientationally averaged shear modulus G, and its maximum and minimum components, C_{44} and $\widetilde{C}_{44}$, respectively, characterize the material's response to a volume conserving shear deformation. This type of deformation leaves the embedding density unchanged and therefore does not contribute via the embedding functional to the free energy. For this reason the shear moduli scale with the two

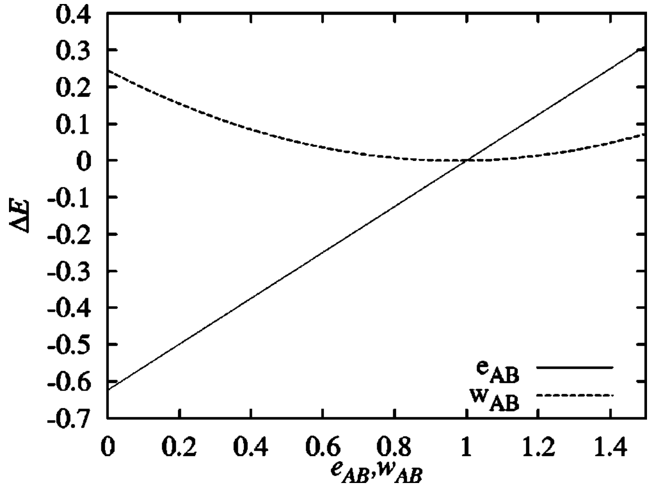

FIG. 8. Effect of GEAM parameters $e_{\rm AB}$ and $w_{\rm AB}$ on the alloy heat of solution ΔE for a single substitutional impurity in the fcc crystal lattice.

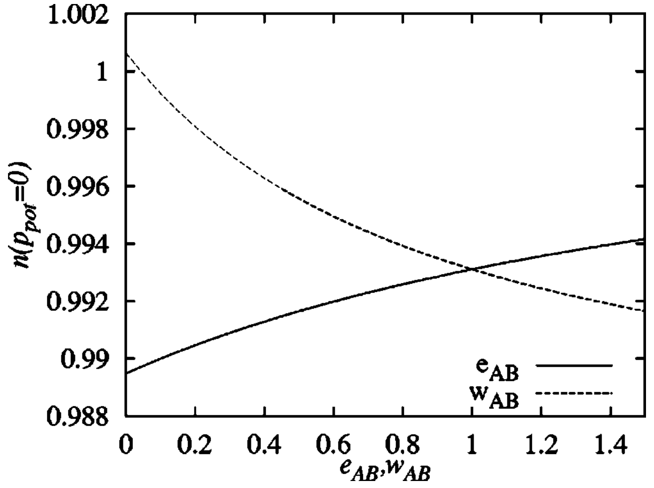

FIG. 9. Effect of GEAM parameters $e_{\rm AB}$ and $w_{\rm AB}$ on the number density $n=N/V$ (reduced units) at zero pressure for a single substitutional impurity in the fcc crystal lattice.

body interaction parameters $e_{\rm AA}$ and $e_{\rm BB}$ linearly, more explicitly, in case of average shear modulus we have $G(e_X) = e_X G(e_X=1.)$ for $X \in \{{\rm AA},{\rm BB}\}$.

D. Doping characteristics

In this section we calculate heats of solution and shear moduli for binary metal systems, and metals with metallic inclusions, where different metals are in contact. To this end we can also demonstrate the usefulness of the polynomial GEAM format.

The heat of solution ΔE for a host bulk material of type A and an inclusion of type B is defined as the change of the total system's energy when an atom of the host material A is replaced by an impurity atom of type B. To estimate the effect of model parameters on the heat of solution in an approximate fashion, we calculate this quantity in the limit of low temperatures using the following procedure: an atom from the bulk is replaced by an impurity; the radial distance to its next neighbors is adjusted so that the (total) isotropic pressure vanishes; the heat of solution is calculated as the difference between total energies between start- and final configurations. For metals with similar crystal lattice constants, within focus of this work (see Table I and Ref. [36]), the true amount of relaxation is small. For that reason also corrections to the approximate values calculated here must be small. Resulting curves are displayed in Fig. 8, where the effect of the strengths $e_{\rm AB}$ and $w_{\rm AB}$ on the heat of solution is presented. For $e_{\rm AB}=e_{\rm AA}=1$, and $w_{\rm AB}=w_{\rm AA}=1$ there is no difference between impurity and material, thus ΔE vanishes in that limit. The heat of solution increases linearly with $e_{\rm AB}$ as the binary interaction potential does. From Fig. 9 we see that the density corresponding to zero pressure increases with $e_{\rm AB}$ as a result of the mismatch between zero pressure densities for systems interacting solely via binary and embedding interactions, respectively. The size of $w_{\rm AB}$ influences the value of the embedding density (ρ) at the impurity location in such a way that it is decreasing with decreasing $w_{\rm AB}$. As result, the number density (n) around an impurity increases with increasing difference $|w_{\rm AB}-w_{\rm AA}|$ in order to achieve the desired vanishing isotropic pressure; cf. Fig. 9. The heat of solution increases with the absolute distance $|w_{\rm AB}-w_{\rm AA}|$ due to the parabolic form of the embedding functional; see Fig. 9.

E. Dimensionless units

When implementing the GEAM model and solving it numerically, any measurable quantity Q with physical dimension $[Q]={\rm kg}^\alpha\,{\rm m}^\beta\,{\rm s}^\gamma$ specified in SI units kg, m, and s is made dimensionless by a reference quantity $Q_{\rm ref} = m^{\alpha+\gamma/2} r_0^{\beta+\gamma} \phi_0^{-\gamma/2}$, such that $Q=Q_{\rm dimless}Q_{\rm ref}$. Dimensionless quantities ($Q_{\rm dimless}$) in this manuscript are therefore always given in terms of these "reference (Lennard-Jones) units." The quantities m, r_0, and ϕ_0 provide the scales via the interaction potential Eq. (3) and the equations of motion. The reference values for length, particle number density, energy, temperature, time, shear rate, pressure (or elastic modulus) in terms of the simulation parameters are therefore $r_{\rm ref}=r_0$, $n_{\rm ref}=r_0^{-3}$, $e_{\rm b,ref}=\phi_0=k_B T_{\rm ref}$, $t_{\rm ref}=r_0(m/e_{\rm b,ref})^{1/2}$, $\dot\gamma_{\rm ref}=t_{\rm ref}^{-1}$, and $P_{\rm ref}=\phi_0 r_0^{-3}=n_{\rm ref}e_{\rm b,ref}$, respectively. By choosing $T_{\rm ref}=\phi_0/k_B = 40$ kK, $P_{\rm ref}=40$ GPa one obtains $\phi_0=3.45$ eV, $n_{\rm ref} = 72.5\ {\rm nm}^{-3}$, and $r_0=0.24$ nm, for GEAM. For $0.8 < e_{\rm AB} < 1.2$ and $0.4 < e_{\rm AB} < 1.5$ the alloy heats of solution of GEAM metal are within the range expected for real metals; cf. Table I. Atomic masses of most metals are within the range $m=(0.8-3.5)\times 10^{-25}$ kg, thus a reference time is $t_{\rm ref} \approx (0.9-2.0)\times 10^{-13}$ s. Constitutive properties and heats of solution are given in Table I for three pairs of metals with similar lattice constants (Cu—Ni, Ag—Au, Pd—Pt).

III. SIMULATION DETAILS

A. Algorithm

Simulations are carried out in a three dimensional, cubic simulation box. The force acting on particle i is obtained by variation of the energy $\delta E_b = \boldsymbol{F}_i \cdot \delta \boldsymbol{r}^i$ of Eq. (1), and reads

$$\boldsymbol{F}^i = \sum_{j \neq i} \boldsymbol{F}^{ij}, \tag{8}$$

$$\boldsymbol{F}^{ij} = - e_{ij} \left. \frac{\partial \mathcal{U}}{\partial \boldsymbol{r}} \right|_{ij} - w_{ij} \left(\left. \frac{\partial \mathcal{F}(\rho)}{\partial \rho} \right|_{i} + \left. \frac{\partial \mathcal{F}(\rho)}{\partial \rho} \right|_{j} \right) \left. \frac{\partial w}{\partial \boldsymbol{r}} \right|_{ij}.$$

Particles move according to Newton's equations of motion, which are second-order ordinary differential equations solved numerically in subsequent time steps using a standard velocity-Verlet algorithm with the forces from Eq. (8) [37]. A suitable integration time step is $\Delta t = 0.01$ [reduced Lennard-Jones (LJ) units] for a metal at room temperature. A cubic simulation box with periodic boundary conditions is used. The central box represents just a fragment of an asperity. For this reason, the properties of the system like overall density, shear, gradient, and temperature are taken to be constant within the simulation cell. To impose a shear deformation (or flow), periodic images are subjected to a relative motion in the flow (x) direction, with a shear gradient in the y direction (Lees-Edwards boundary conditions). The flow simulation introduces the shear rate $\dot{\gamma} \equiv \partial v_x / \partial y$ as an independent variable. While a linear flow profile is observed in steady shear, during the transition towards a steady state, parts of the system move in blocks. To seriously handle simulations with pluglike structures, we implemented a "profile unbiased thermostat" (PUT) which calculates the mean flow velocities self-consistently [38]. The kinetic temperature is introduced through peculiar velocities of particles, $\boldsymbol{C}^i \equiv \dot{\boldsymbol{r}}^i - \boldsymbol{v}(\boldsymbol{r}^i)$, where $\boldsymbol{v}(\boldsymbol{r}^i)$ denotes the (macroscopic) flow velocity on position of particle i:

$$\frac{m}{2} \sum_i (\dot{\boldsymbol{r}}_i - \boldsymbol{v}(\boldsymbol{r}_i))^2 = \frac{3}{2} N k_{\mathrm{B}} T. \tag{9}$$

Peculiar particle velocities are seen as thermal fluctuations and suppressed by the thermostat. The first method carrying out a simulation under strongly controlled conditions was the velocity scaling algorithm proposed by Woodcock [39], which conserves a canonical distribution (see Ref. [40]), if after each integration step, velocities are scaled to satisfy the constant kinetic energy condition. The efficient procedure is easily implemented. Further details of this temperature control method are given elsewhere; see Refs. [41,42]. Alternatively, shear flow can also be generated by modifying the equations of motion with a SLLOD algorithm [43,44]. One should note that NEMD simulations of sliding interfaces have a minimum shear rate below which computational costs become expensive. For particular low rates, alternate simulation strategies, employing transient time correlation functions [45], evaluating differences between equilibrium and nonequilibrium trajectories [46], or beyond equilibrium molecular dynamics [47] may be considered.

Boundary conditions potentially effect the newly formed crystal structure. Crystal planes tend to contain a multiple of unit crystal cells between the boundaries of the system. This results in a deviation between densely packed planes and planes normal to the flow gradient, potentially increasing the probability for the appearance of defects at finite size. We studied several system sizes to make sure that the presented results are not artificially driven by finite size effects. Yield stress and the frequency of defects formed in the steady state shear regime depend via the energy needed to form a defect on the system size; see Ref. [48]. Thus it is important to use a sufficient large number of particles ($N > 5000$) to obtain reliable information about dislocation formation, dynamics, and microstructure generation. Values for the isotropic pressure are estimated from the penetration hardness, defined as the ratio between load N and contact area A at onset of plastic flow. For most metals, the penetration hardness lies in the range 0.005–0.0025 (reduced LJ units); cf. Refs. [49,50]. The dry solid friction process is characterized by large relative velocities at the interface. In simulations presented here the relative velocity is about $0.01 c_{\mathrm{T}}$ (the shear rate is $\dot{\gamma} = 0.001$), where c_{T} is the transverse sound speed. Thus for the GEAM medal, the relative velocity is of the order of 30 m/s. Such high velocities are expected for example in case of thread breaking [51–53]. The time scale of a solid friction process is estimated by the size of an average asperity and velocity, leading to a value of approximately 100 ns. The typical length of a simulation run is 10^4 time units which corresponds to a total simulation time of about 2 ns. The total stimulation time represents only a fraction of the time scale of the friction process. However, as shown in Sec. IV A the stationary state structure is reached soon after onset of the shear flow and enables us to obtain a picture about interplay between the microstructure, dislocation dynamics, material mixing, and flow properties (stress tensor, effective shear rate). The MD simulations with simulation times up to 2.5×10^4 and with different initial configurations (e.g., amorphous, with parallel slip ($[1\bar{1}0]$) and shear directions, and extended in gradient directions) are performed to ensure that processes that might dominate shear deformation are recognized properly during the limited time window of the MD simulations to be discussed.

B. Common neighbor analysis

The common neighbor analysis method based on planar graphs is utilized here to obtain information about the local order within NEMD atomic configurations. This method relies on a suitable definition for "relevant" neighbors [54]. Pairs of atoms are considered to be relevant neighbors, if they are within distance of the first pair correlation function minimum. The diameter of the second coordination shell for a bcc structure is just 15.47% larger compared with the diameter of its first shell. Already at low temperatures atoms from these two shells are mixing, for the bcc structure we therefore have 14 relevant neighbors. For fcc and hcp we have 12 relevant neighbors, i.e., the ones in the first coordination shell, because, in contrast to bcc, the above value is sufficiently large (41.4%). The method is stable against density fluctuations and minor structural changes as discussed in Ref. [54]. Polyhedra formed by relevant neighbors are translated into planar graphs with polyhedra edges as branches and neighbors as nodes. Since these graphs contain only information about connections, orientation, and thermal displacements of the crystal structure do not influence the

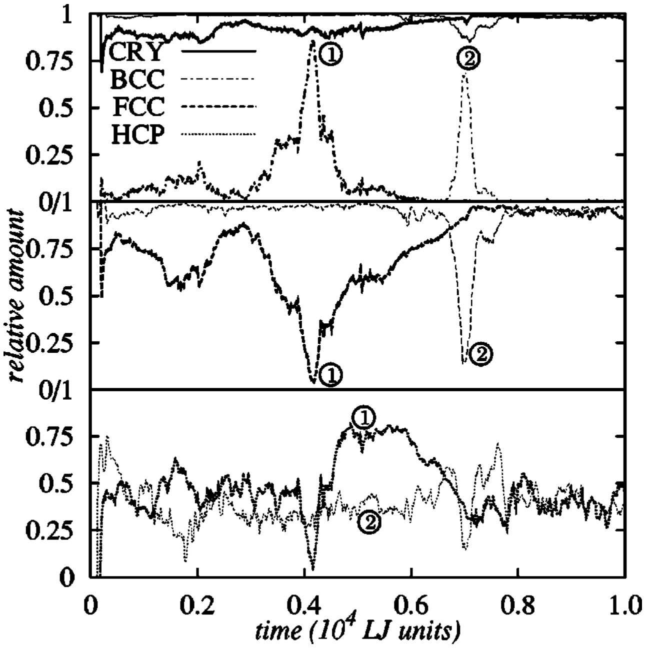

FIG. 10. Relative amount of volume occupied by fcc, bcc, and hcp structures vs time. The bold curve (cry) represents the amount occupied by all three crystalline structures together obtained via NEMD simulation of a homogeneous GEAM metal subjected to steady shear. Initially, particles are placed at ideal fcc lattice sites with the x,y,z axes corresponding to [100], [010], [001] (thicker curves, system ①) and [111], $[22\overline{1}]$, $[1\overline{1}0]$ (thinner curves, system ②) directions in the fcc lattice.

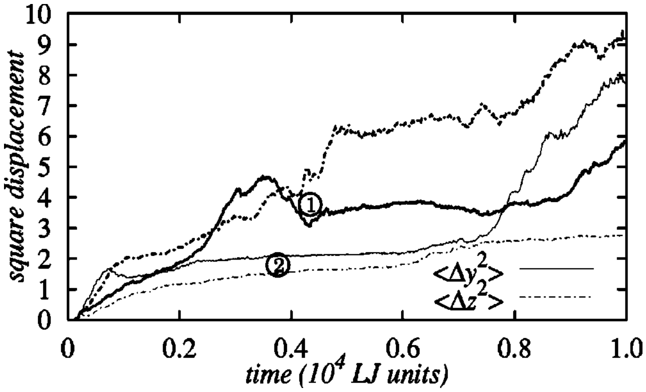

FIG. 11. Average square displacement of particles projected to velocity gradient direction (y), and vorticity direction (z). Initially, particles are placed at ideal fcc lattice sites with the axes x,y,z corresponding to [100], [010], [001] (thicker curves, ①) and [111], $[22\overline{1}]$, $[1\overline{1}0]$ (thinner curves, ②) directions in the fcc lattice.

analysis. The obtained planar graphs are compared with planar graphs of ideal bcc, fcc, and hcp crystal structures. The method resolves the local structure surrounding each atom. For the choice of parameters made here all the three crystal structures are observed. The ratio between all atoms which belong to a structure (central atom plus its neighbors, no double counting) and total number of atoms in the system is taken as a measure for the amount of this crystal structure. Domains with different crystal structures can overlap, therefore the total amount of crystallinity (cry) is not just the sum, but often less, than the amounts separately occupied by fcc, bcc, and hcp structure; cf. Fig. 10(a).

IV. METAL-METAL (GEAM-GEAM) CONTACTS SUBJECTED TO SHEAR

In this section we present results for three different types of metal-metal contacts subjected to shear. While the two materials are characterized by $e_{\mathrm{AA}}, w_{\mathrm{AA}}$, and $e_{\mathrm{BB}}, w_{\mathrm{BB}}$, respectively, the interface is characterized by the strength of the binary interaction parameters e_{AB} and w_{AB}. We begin with studying the “homogeneous” case of a clean, and dry, metal-metal contact, where all the six interaction strengths are equal and set to unity (Sec. IV A). Here, the interface arises due to initial conditions. In order to understand the effect of the interaction strengths on the dynamical behavior, we study two inhomogeneous cases upon varying a single interaction strength in both cases. In Sec. IV B, atoms of different model metals feel an extra attraction due to the embedding term and we choose $w_{\mathrm{AB}} \neq 1$. In Sec. IV C two materials with different shear moduli are in contact, i.e., we set $e_{\mathrm{BB}} \neq 1$ (while keeping $e_{\mathrm{AB}} = e_{\mathrm{AA}}$).

For all three cases, a contact zone at relative motion in the x direction, with a load and shear gradient in the y direction is simulated. The temperature $T=0.01$ and density $n=1$ are held constant. The initial positions of the particles are fcc lattice sites, where axes x,y,z correspond to the directions in starting crystal configuration: [100], [010], [001], and [111], $[22\overline{1}]$, $[1\overline{1}0]$, denoted with ① and ②, respectively. Simulations are performed with $N_{①}=43\,200$ and $N_{②}=48\,668$ particles. In the latter case, the shear direction is orthogonal to the slip plane. The shear rate is $\dot{\gamma}=0.001$. The shear deformation is switched on at $t=0$. In our simulations of shear at the interface between two blocks of different metals, we use homogeneous GEAM configurations, presheared for 4000 time steps, as startup. Each particles’ type is set according to the side of the interface where it resides at $t=0$; type A is assigned to particles with negative y coordinates. At the boundary in the y direction there is an artificial interface. Particles crossing this interface change type.

A. Clean metal$_A$-metal$_A$ contact

First, we consider dry solid friction between two blocks made of identical GEAM material, i.e., $w_{ij}=e_{ij}=1$ for all $i,j \in \{A,B\}$. After the shear deformation is switched on, the system responds with growing shear stress. After reaching a yield stress at $t_{①}=180$, $t_{②}=110$ (reduced units), we observe a sudden increase of the amount of hcp structure as demonstrated in Fig. 10. Atoms move into the nearest potential minima, causing shear of the crystal planes in oblique to the shear flow direction. Layers of hcp structure are formed, and tend to block the flow. During continued shear significant structural changes start to appear. The rearrangement of the crystal structure is followed by an increase of self diffusion, or self mixing, of atoms. In Fig. 11, the average squared displacement of particles with respect to the shear gradient

(y) direction and (vorticity, z) direction normal the shear x-y plane is plotted. These quantities do not only define the diffusion coefficient, but also monitor the amount of interpenetration of particles across the interface. After approximately 1000 time units a stationary structure is formed. The particles are packed in hexagonal layers stacked along the gradient direction to maximize the distances between particles as they shear past each other, and to reduce resistance to shear; cf. Sec. II C. For the chosen set of simulation parameters, fcc and hcp structures are stationary state structures [54]. In the course of the structural rearrangement particles move in average for ≈ 1.3 reduced lengths units in shear direction, what is equivalent to ≈ 1.5 hexagonal layer distances. For the fcc structure the most densely packed planes correspond to the (111) plane, and slip occurs in $[1\bar{1}0]$ direction. The corresponding plane and direction in a bcc structure is $(01\bar{1})$ and [111], respectively. The shear direction is closely parallel, but definitely nonparallel, to the nearest neighbor (slip) direction of the newly formed structure; cf. Fig. 14 at $t=6500$ for system ①. The shear direction projects onto the point $(\varphi,\theta)=(\pm\pi/2,\pi/2)$. A deviation between the steady state shear direction and the fixed flow direction results in a small increase of the average square displacement with time. If the particles are moving back in direction of their starting position (in y or z direction), the average square displacement can also decrease. The long time self-diffusion behavior, however, still remains unresolved within the actual simulation times.

Shear deformation inherently generates defects since atoms can move oblique to the shear direction to reach some close-by energetically preferred states. Even when a stationary flow situation is reached, defects blocking the flow are observed. These defects should be responsible for the difference between the observed amounts of hcp and fcc structures. Though they possess the same energy per particle in the limit of low temperatures, and occur together as randomly close packed structures, in our simulations the fcc structure shows up to be dominant. The explanation should be that the hcp structure allows shearing only in a single plane and that it is less resistant to defects, as compared to fcc. After a defect, partially or completely blocking the flow, is formed, parts of the system move as blocks. Shear stress is then released locally, yielding very high effective shear rates. We observed effective shear rates up to $10\dot{\gamma}$ around $t=5000$ in both systems, cf. Fig. 12. The material between blocks is moving fast in densely packed layers, and blocks are carried with the flow. Thus the increase of the effective shear rate alone does not result in larger average square displacements of particles. The quasiperiodic spikes of the shear stress and square deviation of the flow velocity from a linear profile indicate the existence of stick-slip motion in the system ①; cf. Fig. 12. The period between two spikes is ≈ 100 time units. During this process, in a first step the shear stress accumulates inside the blocks and the velocity profile is mostly linear. In a second step, after slip starts, the accumulated shear stress is released in a thin layer between blocks. Earlier simulations of dry sliding friction between a single Ni asperity and a Cu surface show similar behavior: kinetic energy is converted into potential energy and stored as "strain energy" [9]. Energy stored during stick is released to generate local phonons and later dissipated in the system. The stick-slip motion observed here is the property of those thin layers which interact strongly with the substrate [12].

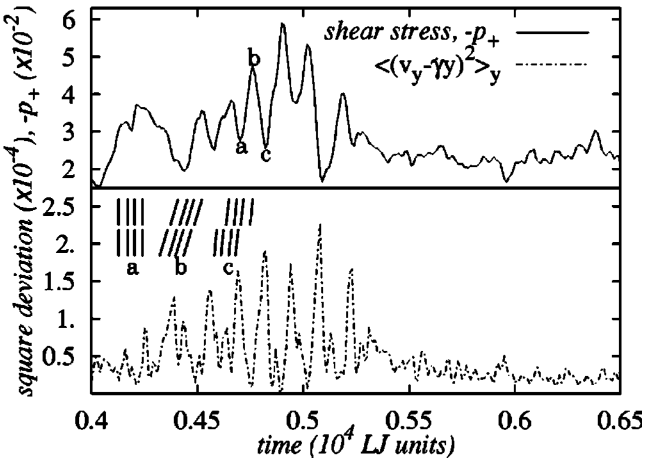

FIG. 12. Section of a long simulation run for system ① showing stick slip motion. Values for shear stress $(-p_+)$ (top) and average square deviation of velocities from a linear profile (bottom graph). Data obtained via NEMD with 43 200, 48 668 particles at density $n=1$, temperature $T=0.01$, and shear rate $\dot{\gamma}=0.001$. Nonequilibrium molecular dynamics simulation results for homogeneous GEAM metal subjected to steady shear. In starting configurations particles are placed at the ideal fcc lattice sites with the axes x,y,z corresponding to [100], [010], [001].

The kinetic and potential contributions to the pressure tensor can be computed separately via NEMD. The kinetic part of the scalar pressure is, due to temperature control, given by $p_{\text{kin}}^{\text{iso}}=nk_{\text{B}}T$ and of the order of the potential contribution to the scalar pressure. The kinetic contributions to the shear stress $(-p_+)$ and normal pressure differences $(p_{-,0})$, however, are negligible compared with the potential counterparts (of the order of 0.1%), as for dense fluids [55]. At $t=6000$ we observe an effective shear rate $\approx 2\dot{\gamma}$ for both systems. Simultaneously, we observe that the shear stress and its fluctuations decrease. The explanation should be that different modes of collective motion of densely packed hexagonal layers yield different average shear stresses; see Sec. II C. Also, the existence of different shear modes should be responsible for slow changes of the shear stress in time. Normal pressure differences, however, are close to zero, and their behavior shows little connection with the intermediate flow properties. We observe a change of the normal pressure differences only if the system cannot globally adjust itself to accommodate shear deformation.

The normal pressure difference p_- increases sharply in Fig. 13 (thinner curve), after a defect is formed at $t=6600$ in the system ②. Increase of p_- is followed by a structural transformation of parts of the fcc structure into bcc structure and a decrease of isotropic pressure. The isotropic pressure decreases since at the same temperature and density the bcc structure has negative isotropic pressure (cf. Figs. 10 and 13). Under structural transformation the original slip (111) plane/$[1\bar{1}0]$ direction of the fcc structure transform into $(01\bar{1})$ plane/[111] direction, of the bcc structure; see Fig. 14.

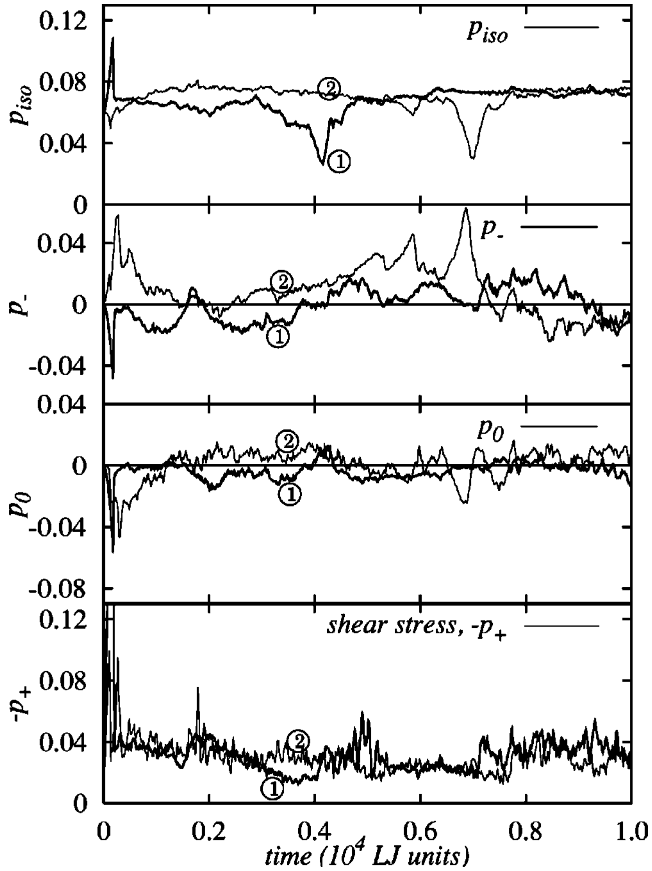

FIG. 13. Evolution of the isotropic pressure p_{iso} and the three components of the anisotropic pressure tensor $p_{+,-,0}$ with time; cf. Sec. II C for definitions. Results are obtained via NEMD with 43 200, and 48 668 particles at number density $n=1$, temperature $T=0.01$, and shear rate $\dot{\gamma}=0.001$ for a homogeneous GEAM metal subjected to steady shear. Initially, particles are placed at ideal fcc lattice sites with the axes x,y,z corresponding to [100], [010], [001] (thicker curves, system ①) and [111], $[22\bar{1}]$, $[1\bar{1}0]$ (thinner curves, system ②) directions in the fcc lattice.

We could not simply classify this structure transformation into one of the basic mechanisms described in Sec. II B. The available results suggest, that both mechanisms are locally present. During the transformation of bcc structure back into fcc structure, parts of the system transform along several different directions. Snapshots of the system ② during the transformation (around $t=7000$) are presented in Fig. 15 where domains with different structures can be observed. At $t=7500$ the fcc structure is recovered, a number domains with different orientations are visible and the large-scale structure is oriented to block the flow; see Fig 15. These domains rotate with the flow (vorticity). After $t\approx 8000$, the system is again partially aligned with the flow but different domains are still visible; see Fig. 14. The rotation of domains is characterized by a steep increase of the average square displacement in flow gradient (y) direction, while the displacement in the neutral (z) direction is small. During 2500 time units domains move in y direction for $\approx$2.5 layer distances ($\langle \Delta y^2 \rangle \approx 5.4$). In Ref. [13], a similar behavior was observed for a two-dimensional embedded atom model metal-metal interface. The mixing of the material at the interface was closely related with the fine-grained microstructure, which is created during the shear.

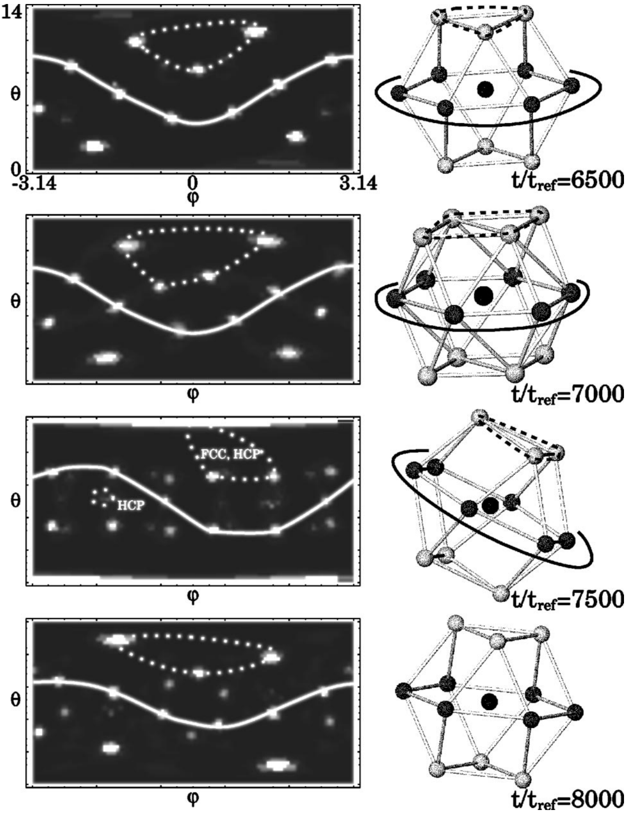

FIG. 14. Angular distribution of directions to closest neighbors during the transformation between fcc and bcc crystal structures. Snapshots are obtained via NEMD with 43 200 particles (system ①). Simulation parameters are: $T=0.01$, $\dot{\gamma}=0.001$, and $n=1$. Starting configuration is the ideal fcc structure, the flow, gradient, and vorticity directions correspond to [111], $[22\bar{1}]$, $[1\bar{1}0]$ crystal directions, respectively. The nodes represent neighbors and they are connected with an edge if they are neighbors with themselves. Atoms in slip planes are marked by bold lines. In this representation, the shear direction projects at points $(\varphi,\theta)=(\pm\pi/2,\pi/2)$.

B. Metal$_A$-metal$_A$ contact with additional embedding interaction

If the interfacial embedding interaction parameter $w_{\mathrm{AB}} \neq 1$ is different from the embedding interaction parameters within the bulk $w_{\mathrm{AA}}=w_{\mathrm{BB}}=1$ the local density changes in the vicinity of impurities. The effect of this binary embedding interaction in the limit of low temperatures is discussed in Sec. II D. For GEAM, the local number density $n=N/V$ is close to the embedding density ρ calculated from Eq. (2). Figure 16 shows the the evolution of the number density $n \approx \rho_A+\rho_B$ within the interfacial layer between two model metals for $w_{\mathrm{AB}}=0.3$, 0.5, and 1.3 (three cases). Embedding densities ρ_A, ρ_B are calculated for each particle type separately for each point at a square grid. The interface, inclusions, and vacancies formed during shear are visualized through the measure $\rho_A-\rho_B$.

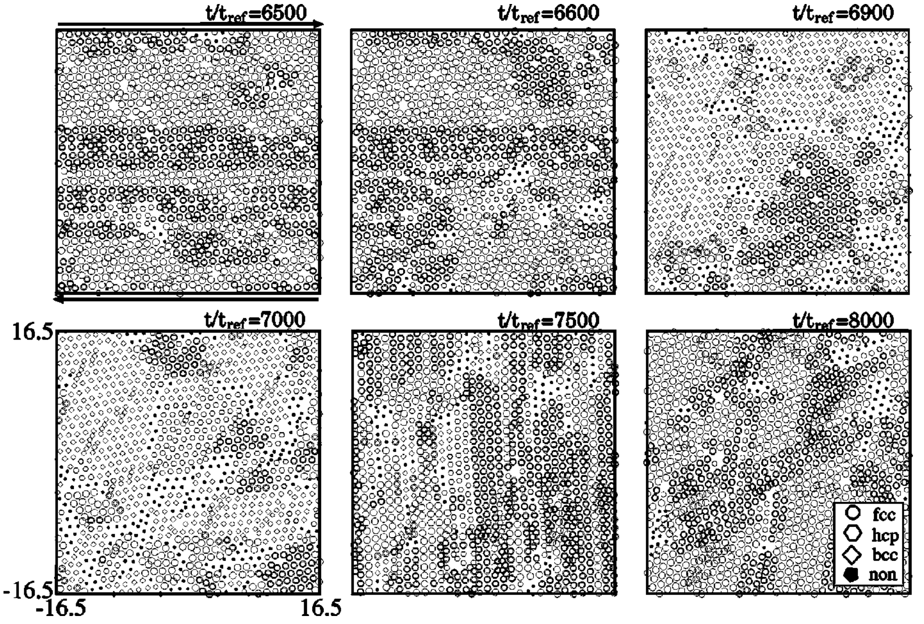

FIG. 15. Snapshots visualizing the evolution of structure during temporary transformation of crystal structure from fcc into bcc. Snapshots are obtained via NEMD with 43 200 particles (system ①). Each slice has a depth of unity. Simulation parameters are: $T=0.01$, $\dot{\gamma}=0.001$, and $n=1$. The [111], $[22\bar{1}]$, $[1\bar{1}0]$ directions in the starting configuration, a fcc crystal lattice, correspond to shear flow direction, gradient direction, and direction of normal to the shear plane, respectively. The type of local structure is indicated. The shear direction is indicated in the upper left picture. As before, all quantities are expressed in dimensionless LJ units.

The density inside the bulk material is constant and similar in all these (three) cases. At the interface, we observe changes in the local number density. The system minimize the embedding energy locally by changing the embedding density such that it matches the desired embedding density; cf. Eq. (5). This results in an increase of the local density for $w_{\mathrm{AB}}=0.3$. 0.5 (light line in Fig. 16) and a decrease for $w_{\mathrm{AB}}=1.3$ (dark line). For $w_{\mathrm{AB}}=0.3$, after a defect—followed by Burgers transformation—is formed at $t=7200$, the part of the system located around the contact plane starts to rotate with the shear flow to form an inclusion. The microscopic inclusion produced in sliding penetrates for about three length units into the other material block. This process results in mechanical alloying at the interface since the parts of the inclusions move with different relative speeds in shear direction due to the flow gradient. For cross sections taken at $t=11\,000$ see Fig. 16. Similar behavior is observed for $w_{\mathrm{AB}}=1.3$. For $w_{\mathrm{AB}}=0.5$, the slip direction of the crystal structure is nonparallel with the interface. This leads to a gradual alloying of two materials parallel to the interface. We also observe in Fig. 16, vacancies created during the shear flow as black spots in the $\rho_A+\rho_B$ density plots. Their vacancy is typically two atoms wide and has a life time between 50 and 400 time units. They appear with and without defects and tend to be aligned with the flow.

Within statistical errors, we did not detect an influence of the (additional) embedding interaction on the shear stress and normal pressure differences. This is plausible, because the interface occupies only a small portion of total volume and pressure tensor components reflect the material flow within the whole system.

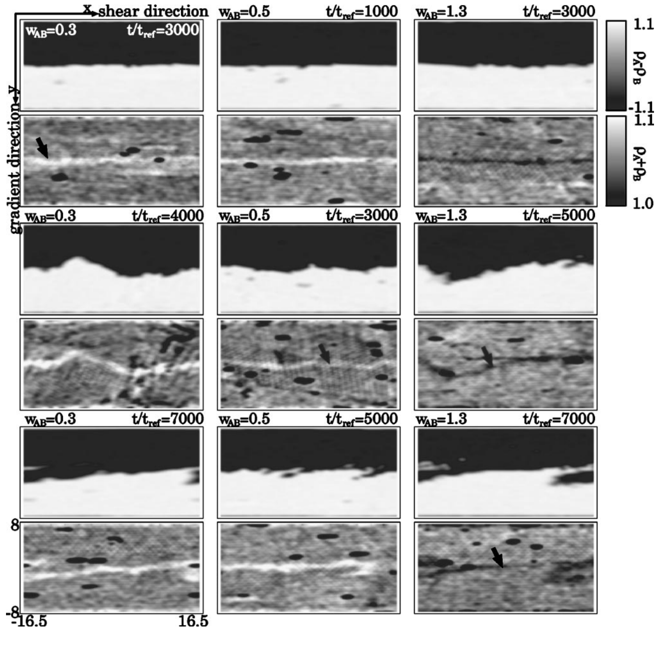

FIG. 16. Cross section of the embedding density close to the interface, averaged over a time period $\Delta t=200$ for three values of the GEAM parameter w_{AB} (arranged in columns) and three different times (arranged in rows). The local density ρ is estimated from the sum of embedding densities of the two materials ρ_A,ρ_B, $\rho\approx\rho_A+\rho_B$ (lower, more structured, nine density plots). Embedding densities ρ_A,ρ_B are calculated for each type of particles separately for all points at a grid. To visualize and resolve inclusions and vacancies at the interface the quantity $\rho_A-\rho_B$ is used (upper density plots). The NEMD configurations are sampled after every ten time units. Simulation parameters in LJ units are: $T=0.01$, $\dot{\gamma}=0.001$, and $n=1$.

C. Metal$_A$-metal$_B$ contact

The form of the EAM allows to systematically vary shear moduli, i.e., resistance to shear deformation, with strength of two body interaction parameters: e_{AA}, e_{AB}, and e_{BB}; see Sec. II D. We choose $e_{\mathrm{BB}}=1$. (basic GEAM metal) and vary e_{AA}, while $e_{\mathrm{AB}}=e_{\mathrm{AA}}$. After onset of shear flow, an inhomogeneous shear profile is established; cf. Fig. 17. We observe that the mechanical alloying at interface depends on the shear moduli of the two materials. If the absolute difference between their

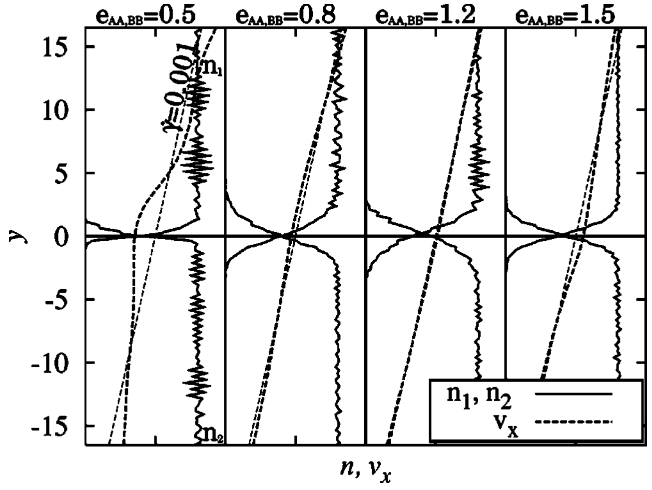

FIG. 17. Mean flow velocity profile for cases, where two materials with different two body GEAM interaction parameters $e_{AA}=e_{AB}=0.5$, 0.8, 1.2, and 1.5 (while $e_{BB}=1$) are in contact. The four samples exhibit different ratios between shear moduli of the two interacting materials $G_1/G_2=0.5$, 0.8, 1.2, and 1.5, respectively. The velocity profiles are averaged over the time frame $t=3000-7000$. All systems have 43 200 particles. For the same systems sample density profiles for both types of particles are given at time $t=6000$. The shear rate is $\dot{\gamma}=0.001$ and temperature $T=0.01$. All quantities are given in LJ units.

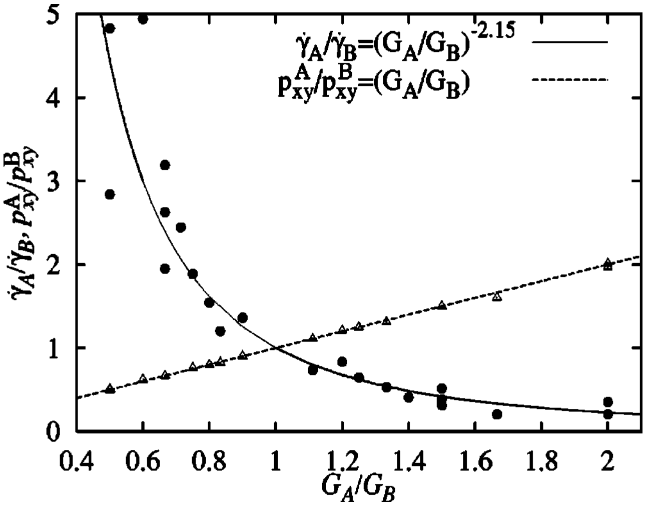

FIG. 18. Ratio of effective shear rates $\dot{\gamma}_A/\dot{\gamma}_B$ (full line) and corresponding shear stresses $p^{\mathrm{A}}_{\mathrm{xy}}/p^{\mathrm{B}}_{\mathrm{xy}}$ (broken line) vs the ratio of shear moduli G_A/G_B in materials of types A and B. Symbols denote averages from the simulation of an interface for shear rate $\dot{\gamma}=0.001$ and temperature $T=0.01$ with 43 200 particles. The shear moduli are controlled via the GEAM parameters e_{AA} and e_{BB}, where $e_{AB}=e_{BB}$. Curves are drawn to guide the eyes.

shear moduli is large (here $e_{AA}=0.5$ or 2), the shear is concentrated in the material with smaller shear modulus while the other material moves almost as a block. For this reason we observe mixing of the two metals only within a single hexagonal layer at the interface. If shear moduli are comparable (here $e_{AA}=0.8$, 1.2) we observe that both materials penetrate for ≈3 hexagonal close packed layer distances behind the interface (here, after 8000 time units). The dependence of the ratio of effective shear rates $\dot{\gamma}_A/\dot{\gamma}_B$ on the ratio of shear moduli G_A/G_B for metals A and B is presented in Fig. 18. We tested a simple hyperbolic relationship between them, where the coefficient is obtained via regression. Since the shear stress and moduli have the same origin (traced back to the shape of two body interaction potential), the observed ratio of shear stresses equals the ratio of shear moduli, i.e., $p^{\mathrm{A}}_{\mathrm{xy}}/p^{\mathrm{B}}_{\mathrm{xy}}=G_A/G_B$. We find that only the ratio of shear moduli influences the local shear stress and effective shear rate. This should be a consequence of the strong dependence of local shear stress on the mode of collective motion (amplitude of zigzag motion; cf. Sec. II C).

The analysis of the crystal morphology at $t=4000$ is presented in Fig. 19. In case $e_{AA}=e_{AB}=0.5$, the bcc structure is the dominant stationary structure for metal$_A$ particles at $T=0.01$ and $\dot{\gamma}=0.001$. In the limit of low temperatures the fcc structure is preferred in metal$_A$. The difference between energies per particle in bcc and fcc structure, $(E_{\mathrm{c,bcc}}-E_{\mathrm{c,fcc}})$, decreases with the strength of the two body interaction parameter e_{AA}. In Ref. [21] it is shown that the bcc structure can be additionally stabilized by entropy contributions to the free energy. To make this more visible we also provide the angular distribution of directions to next neighbors of dominant structures for two of the dominant structures on the right side of Fig. 19. It is visible that two-dimensional densely packed layers in bcc and fcc structures are parallel and shear such that they pass each other. In the two remaining cases, for $e_{AA}=e_{AB}=0.8$, 1.2, the fcc structure becomes stationary within the whole system. Mechanisms of mechanical alloying are similar to the case where we exploited the additional embedding interaction ($w_{AB}\neq 1$). Again, we observe a temporary transformation of parts of the system into bcc structure; cf. Fig. 19 for $e_{AA}=e_{AB}=1.2$.

V. CONCLUSIONS

In this paper we explored several dynamical and structural, equilibrium, and nonequilibrium, properties of a simple embedded atom model. The model helps us to understand and predict processes taking place during dry solid friction between metal-metal interfaces. The initial configuration massively changed under the applied shear. A re-ordering of particles takes place: particles create hexagonal layers orthogonal to the flow gradient direction. The shear deformation involves motion of these planes. In the steady state regime, defects are created when atoms move oblique to the shear direction to reach some close-by energetically preferred states. These defects potentially block the shear flow and lead to shear banding. While the total amount of crystallinity during the simulation is fairly constant (quantified via common neighbor analysis), the fcc structure partially transforms, as long as defects blocking the flow are present, into the bcc structure. During these processes, transient, grained microstructures are created. Related to the grain formation is the mixing of the material through rotation of the grains

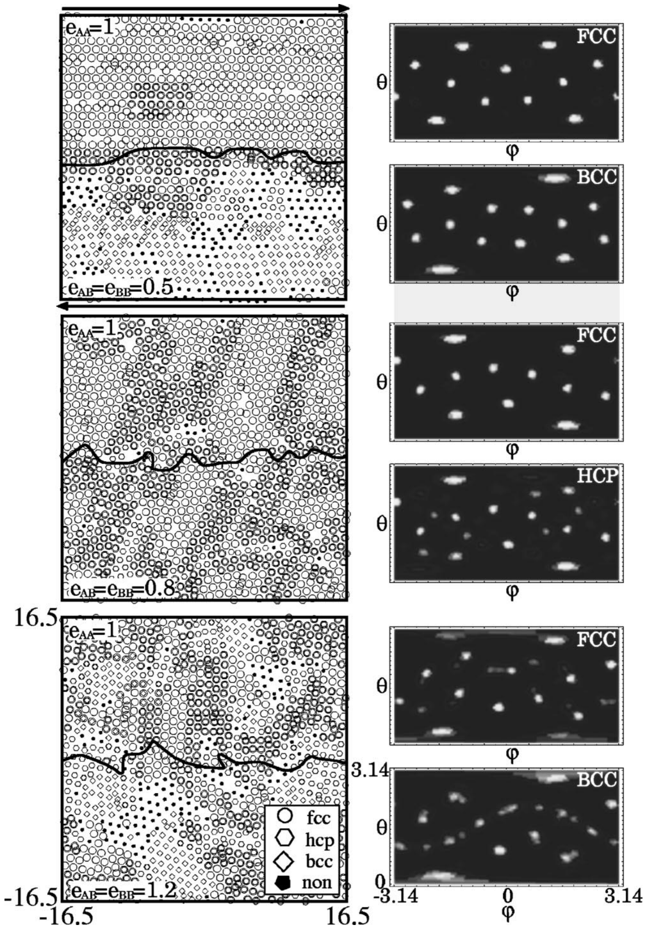

FIG. 19. Structural snapshots (left) at the interface of two materials. Shown are systems with three different shear moduli at time $t=4000$ (reduced units). Corresponding parameters are $e_{\mathrm{AA}}=1$ and $e_{\mathrm{AB}}=e_{\mathrm{BB}}=0.5$, 0.8, and 1.2 (from top to bottom). Snapshots are obtained via NEMD with 43 200 particles. Each slice has a depth of unity. The angular distribution (right) of directions to the closest neighbors is provided for the dominant structures.

before the system re-enters a dynamically equilibrated (stationary) state. The structural information also helps to interpret the observed changes of the pressure tensor. We could show, that the isotropic pressure is mainly determined by the (instantaneously) dominating crystal structure. Normal pressure differences are close to zero during most simulation runs. Nonvanishing normal pressure differences occur if defects (blocking the flow) are created which the system cannot accommodate. The shear stress is found to depend on the modes of collective motion of atoms stacked into hexagonal planes. The NEMD results for shear stress and normal pressure differences were compared with analytic calculations for collectively moving atoms. In situations, where defects are blocking the flow, except within a narrow slit, stick-slip motion under very high effective shear rates is observed. The stick-slip motion observed in this work is relevant at the "nanoscale." On the level of several asperities, during a dry solid friction process, stick-slip might become coarse-grained and smooth, or trigger stick-slip on larger scales. Conclusions about these mechanisms are obviously out of reach for the present simulations. However, stick-slip on the nanoscale is accessible when sliding a blunt tip over a substrate. In this application shear deformation is confined within several layers around the interface.

The generic embedded atom model has been further extended to study interfaces between different metals with similar lattice constants. We illustrated the dependence of the heat of solution and the local density for a single substitutional impurity on model parameters. The mechanism of mixing (or mechanical alloying) are similar for all three versions of interface: homogeneous, with additional embedding interaction and with different shear moduli. Unexpected at first glance, the additional embedding interaction leads to a pronounced increase in the local density. For the same system, penetration of inclusions through the interface and subsequent mechanical alloying has been observed and discussed. Further, gradual alloying at the interface has been traced back to the mismatch (final angle) between the interfacial plane and shear direction. In this early stage of mechanical alloying, we do not detect an influence of the additional embedding interaction on the shear stress. In our simulations, the area where two materials are mixed occupies only a small portion of the total volume and thus only slightly influences the pressure tensor components. The low degree polynomial format of GEAM comes together with a simple relationship between the strength of the two body interaction and the shear moduli in the limit of low temperatures, which determine the resistance of the system to the shear deformation. We find a dependence between ratios of shear moduli, shear stresses, and effective shear rates in two materials, while the values for moduli, shear stress, and shear rates of the pure materials seem to be (at least in our study) uncorrelated. The explanation should be that modes of collective motion of hexagonal layers are coupled across the material interface.

Interfaces between metals with different lattice constants where potential incommensurabilities increase the number of dislocation types remain to be studied. The features observed in this work should be generic to high-speed friction at the metal-metal interface. Except for very finely polished surfaces, mesoscale inhomogeneities and inclusions are known to play an important role. The recently developed mesoscale grid free simulation techniques offer the potential for modeling metals at larger scales [56–59]. The nanoscale physics discussed in this manuscript provides ingredients to be used by these methods.

ACKNOWLEDGMENTS

Financial support provided by the Deutsche Forschungsgemeinschaft (DFG) via the special research area Sfb 448 "Mesoskopisch strukturierte Verbundsysteme" and the fruitful cooperation with Marco Ellero supported by DFG Project No. HE 1100/7-1 are gratefully acknowledged. Computing resources at the ETH Zürich (dec-unix cluster nodes) have been used.

[1] D. Kuhlmann-Wilsdorf, Wear **200**, 8 (1996).
[2] N. S. Liou, M. Okada, M. A. Irfan, and V. Prakash, Opt. Lasers Eng. **40**, 393 (2003).
[3] Z. N. Farhat, Wear **250**, 401 (2001).
[4] W. R. Patterson and I. G. Greenfield, Acta Metall. **19**, 123 (1971).
[5] C. M. Mate, in *Handbook of Micro/Nano Tribology*, edited by B. Bhushan (CRC, Boca Raton, 1995), p. 167.
[6] *Nanoscience: Friction and Rheology on the Nanometer Scale*, edited by E. Meyer, T. Gyalog, R. M. Overney, and K. Fransfeld (World Scientific, Singapore, 1998).
[7] E. D. Smith, M. O. Robbins, and M. Cieplak, Phys. Rev. B **54**, 8252 (1996).
[8] B. N. J. Persson, Phys. Rev. B **48**, 18140 (1993).
[9] A. Buldum and S. Ciraci, Phys. Rev. B **55**, 12892 (1997).
[10] M. H. Müser and M. O. Robbins, Phys. Rev. B **61**, 2335 (2000); M. H. Müser, L. Wenning, and M. O. Robbins, Phys. Rev. Lett. **86**, 1295 (2001).
[11] O. M. Braun and M. Peyrard, Phys. Rev. E **63**, 046110 (2001).
[12] A. Buldum and S. Ciraci, Phys. Rev. B **60**, 1982 (1999).
[13] J. E. Hammerberg, B. L. Holian, J. Röder, A. R. Bishop, and S. J. Zhou, Physica D **123**, 330 (1998).
[14] I. Stankovic, S. Hess, and M. Kröger, Phys. Rev. E **69**, 021509 (2004).
[15] H. Van Swygenhoven, P. M. Derlet, and A. G. Frøseth, Nat. Mater. **3**, 399 (2004).
[16] E. B. Tadmor and S. Hai, J. Mech. Phys. Solids **51**, 765 (2003).
[17] H. Van Swygenhoven and P. M. Derlet, Phys. Rev. B **64**, 224105 (2001).
[18] J. Schiøtz, T. Vegge, F. D. Di Tolla, and K. W. Jacobsen, Phys. Rev. B **60**, 11971 (1999).
[19] M. Kröger, I. Stankovic, and S. Hess, Multiscale Model. Simul. **1**, 25 (2003).
[20] C. Zener, Phys. Rev. **71**, 846 (1947).
[21] P. J. Craievich, M. Weinert, J. M. Sanchez, and R. E. Watson, Phys. Rev. Lett. **72**, 3076 (1994).
[22] C. Kittel, *Introduction to Solid State Physics*, 2nd ed. (Wiley, New York, 1976).
[23] W. G. Burgers, Physica (Amsterdam) **1**, 561 (1935).
[24] R. M. Wentzcovitch and H. Krakauer, Phys. Rev. B **42**, 4563 (1990).
[25] P. J. Craievich, J. M. Sanchez, R. E. Watson, and M. Weinert, Phys. Rev. B **55**, 787 (1997).
[26] K. Kadau, Ph.D. dissertation, University of Duisburg, Germany, 2001.
[27] P. Entel, R. Meyer, and K. Kadau, Philos. Mag. B **80**, 183 (2000).
[28] S. Hess, M. Kröger, and W. G. Hoover, Physica A **239**, 449 (1997).
[29] Y. R. Wang and D. B. Boercker, J. Appl. Phys. **78**, 122 (1995).
[30] M. S. Daw, Phys. Rev. B **39**, 7441 (1989).
[31] K. Fuchs, Proc. R. Soc. London, Ser. A **153**, 622 (1936).
[32] *American Institute of Physics Handbook*, 3rd ed. (McGraw-Hill, New York, 1972).
[33] R. Hultgren, P. D. Desai, D. T. Hawkins, M. Gleiser, and K. K. Kelley, *Values of the Thermodynamic Properties of Binary Alloys* (American Society for Metals, Metals Park, OH, 1973).
[34] J. A. Zimmerman, H. J. Gao, and F. F. Abraham, Modell. Simul. Mater. Sci. Eng. **8**, 103 (2000).
[35] N. Bernstein and E. B. Tadmor, Phys. Rev. B **69**, 094116 (2004).
[36] R. A. Johnson, Phys. Rev. B **39**, 12554 (1989).
[37] M. P. Allen and D. J. Tildesley, *Computer Simulation of Liquids* (Clarendon, Oxford, 1987).
[38] W. Loose and S. Hess, in *Microscopic Simulations of Complex Flows*, edited by M. Mareschal (Plenum, New York, 1990).
[39] L. V. Woodcock, Chem. Phys. Lett. **10**, 257 (1971).
[40] H. C. Andersen, M. P. Allen, A. Bellemans, J. Board, J. H. R. Clarke, M. Ferrario, J. M. Haile, S. Nose, J. V. Opheusden, and J. P. Ryckaert, Rapport d'activite scientifique du CECAM, Universite Paris Sud, 1984.
[41] S. Hess and W. Loose, Physica A **162**, 138 (1989).
[42] W. G. Hoover, Annu. Rev. Phys. Chem. **34**, 103 (2983); D. J. Evans and G. P. Morriss, Comput. Phys. Rep. **1**, 287 (1984); D. J. Evans and W. G. Hoover, Annu. Rev. Fluid Mech. **18**, 243 (1986).
[43] W. G. Hoover, Physica A **194**, 450 (1993).
[44] D. J. Evans and G. P. Morriss, *Statistical Mechanics of Nonequilibrium Liquids* (Academic, London, 1990).
[45] G. P. Morriss and D. J. Evans, Phys. Rev. A **35**, 792 (1987).
[46] G. Ciccotti, G. Jacucci, and I. R. McDonald, J. Stat. Phys. **21**, 1 (1979).
[47] M. Kröger and H. C. Öttinger, J. Non-Newtonian Fluid Mech. **120**, 175 (2004).
[48] M. F. Horstemeyer, M. I. Baskes, and S. J. Plimpton, Acta Mater. **49**, 4363 (2001).
[49] F. P. Bowden and D. Tabor, *The Friction and Lubrication of Solids*, 2nd ed. (Clarendon, Oxford, 1954).
[50] B. N. J. Persson, *Sliding Friction*, 2nd ed. (Springer, Berlin, 2002).
[51] J. F. Archard, Wear **2**, 438 (1958).
[52] G. J. Moyar and D. H. Stone, Wear **144**, 117 (1991).
[53] M. R. Johnson, R. E. Welch, and K. S. Yeung, J. Eng. Ind. **99**, 18 (1977).
[54] I. Stankovic, M. Kröger, and S. Hess, Comput. Phys. Commun. **145**, 371 (2002).
[55] M. Kröger, Phys. Rep. **390**, 453 (2004).
[56] J. J. Monaghan, Annu. Rev. Astron. Astrophys. **30**, 543 (1992).
[57] L. D. Libersky, A. G. Petschek, T. C. Carney, J. R. Hipp, and F. A. Allahdadi, J. Comput. Phys. **109**, 67 (1993).
[58] B. I. M. ten Bosch, J. Non-Newtonian Fluid Mech. **83**, 231 (1999).
[59] M. Ellero, S. Hess, and M. Kröger, J. Non-Newtonian Fluid Mech. **105**, 35 (2002).